

Human perceptual decision making of nonequilibrium fluctuations

Aybüke Durmaz^{1*}, Yonathan Sarmiento^{1,2}, Gianfranco Fortunato¹, Debraj Das²,
Mathew Ernst Diamond¹, Domenica Bueti^{1†}, and Édgar Roldán^{2‡}

¹*International School for Advanced Studies (SISSA), Via Bonomea 265, 34136 Trieste, Italy*

²*ICTP – The Abdus Salam International Center for Theoretical Physics, Strada Costiera 11, 34151 Trieste, Italy*

Perceptual decision-making frequently requires making rapid, reliable choices upon encountering noisy sensory inputs. To better define the statistical processes underlying perceptual decision-making, here we characterize the choices of human participants visualizing a system of nonequilibrium stationary physical dynamics and compare such choices to the performance of an optimal agent computing Wald’s sequential probability ratio test (SPRT). Participants viewed movies of a particle endowed with drifted Brownian dynamics and had to judge the motion as leftward or rightward. Overall, the results uncovered fundamental performance limits, consistent with recently established thermodynamic trade-offs involving speed, accuracy, and dissipation. Specifically, decision times are sensitive to entropy production rates. Moreover, to achieve a given level of observed accuracy, participants require more time than predicted by SPRT, indicating suboptimal integration of available information. In view of such suboptimality, we develop an alternative account based on evidence integration with a memory time constant. Setting the time constant proportionately to the deviation from equilibrium in the stimuli significantly improved trial-by-trial predictions of decision metrics with respect to SPRT. This study shows that perceptual psychophysics using stimuli rooted in nonequilibrium physical processes provides a robust platform for understanding how the brain takes decisions on stochastic information inputs.

I. PERCEPTUAL DECISION MAKING

A key function of the brain is to process noisy sensory data to make fast and accurate decisions [1]. In the simplest scenario – a binary decision between two competing hypotheses, H_1 and H_2 – Wald’s sequential probability ratio test (SPRT) [2], rooted in probability theory [3], is a plausible universal model for optimal decision making in diverse fields of natural sciences (statistics [4], bio-

physics [5, 6], neuroscience [7–9]). The SPRT accumulates ongoing evidence by computing the log-likelihood probability ratio between H_1 and H_2 until the weight of evidence towards one or the other exceeds a predefined threshold value. In neuroscience, the SPRT has been applied to drift-diffusion models (DDM) [8] wherein a decision is taken as soon as the accumulated log-likelihood ratio —which fluctuates instantaneously but has a net drift— reaches one of the two thresholds. Combining the SPRT and DDM paradigms gives a physical first-passage-time problem in a bounded interval, where the boundary that is first reached (H_1 or H_2), and the exit time from the interval, correspond to the decision and decision time, respectively [10].

A variety of behavioural tasks with rhesus monkeys [11–13], rats [14], and humans [8] yielded actual decision-making outcomes close to the optimal performance predicted by SPRT, lending credence to sequential hypothesis-testing models [1, 15]. One widely-used task involves judging the net motion within a random dot motion (RDM) display on a screen. In one of these studies, rhesus monkeys were trained to respond with a saccade to the side of the screen that matched the perceived net motion (e.g. saccade to the right for net rightward dot motion, saccade to the left for leftward dot motion) [12]. Across trials, the level of direction coherence among moving dots in the selected direction was manipulated, making a given trial easy or hard. The activity of spatially selective neuronal populations in the lateral intra-parietal area (LIP) correlated with monkeys’ decision. For rightward saccades (i.e., rightward choice), for example, 220 milliseconds after the motion onset, activity in LIP neurons coding for the rightward spatial location, gradually increased and peaked around the saccade onset [12]. Activity was similarly suppressed in neurons coding for the leftward spatial location (the non chosen position). Importantly the rate of activity increase or suppression correlated with the coherence of the stimuli i.e., the higher the coherence, the steeper the increase and suppression. Thus the activity of single neurons in area LIP reflects both the direction of a forthcoming saccade and the quality of the sensory information that instructs this response. [1, 11–13, 15]. These findings seem to reveal neuronal operations corresponding to evidence accumulation to a threshold, as proposed by the DDM framework.

Even if DDM models have been successful in uncovering some decision making processes in the brain [8], they fall short in accounting for trial-to-trial differences

*Contributing author: adurmaz@sissa.it

†Corresponding author: bueti@sissa.it

‡Corresponding author: edgar@ictp.it

observed for the same stimulus parameters, i.e. for trials with the identical dot coherence level, but minutely different due to stochastics. By contrast, recent work highlights the relationship between the complex spatio-temporal fluctuations of the stimulus and the inter-trial variability in the decision outcomes [15–23]. In one of these works for example, participants consistently take into account not only the overall noise across a trial, but also the detailed spatiotemporal noise patterns within stimuli [17]. Likewise, the explained performance variability is increased when the model is supplied with the stochastic trajectories of the stimulus rather than with an average-based, nonspecific noise [18, 24].

Human perceptual experiences emerge within a context of external noisy stimuli produced by nonequilibrium physical systems that are characterized by time correlations and thus do not evolve as mere random dots. In order to make timely and effective decisions for survival, living systems must handle physical nonequilibrium fluctuations across scales that are characterized by time irreversibility (e.g. net currents of matter and energy) and energy dissipation. For example, a physically-plausible strategy for a cell to accurately sense extracellular ligand concentrations is through maximum-likelihood estimation [25, 26]. It has also been shown that simple biochemical networks are sufficient to execute the SPRT at the cellular level to e.g. discriminate between two levels of concentrations, two different binding rates, etc [5]. Yet it remains an open question whether principles seen in simple systems will generalize to the macroscopic scale when living organisms perceive fluctuating data generated by nonequilibrium physical phenomena [27]. To answer this question, we designed a human visual perception experiment where volunteers were exposed to movies of a driven Brownian particle described by a Langevin equation with few nonequilibrium degrees of freedom. Data analysis based on stochastic thermodynamics theory establishes a robust linkage between participants' behavioural responses and the input parameters of the physical process. Our multidisciplinary approach combining behavioural psychophysics, decision making computational frameworks, and stochastic thermodynamics paves the way to a refinement of decision-making models beyond the SPRT, and reveals fundamental thermodynamic limits [28] that constrain the response of humans to nonequilibrium stationary stimuli.

II. SEQUENTIAL PROBABILITY RATIO TEST ON THE DIRECTION OF TIME'S ARROW

Consider a time series of snapshots characterized by a nonequilibrium stationary stochastic process X_t . By observing this evidence, one must make a decision D_{dec} by choosing between two competing hypotheses, each corresponding with a physical model of the process, e.g. $H_1 = 1$ and $H_2 = -1$. When judging such a stochastic process in a sequence of independent trials, how

should one process the evidence to *optimally* achieve the minimal decision time (averaged across trials) for a given, prescribed level of accuracy? The first rigorous answer to this question emerges from Wald's SPRT: the optimal decision time T_{dec} for selecting $D_{\text{dec}} = 1$ ($D_{\text{dec}} = -1$) is when the cumulated log-likelihood ratio $\mathcal{L}_t = \ln[\mathcal{P}(X_{[0,t]}|H_1)/\mathcal{P}(X_{[0,t]}|H_2)]$ first exceeds (first falls below) a fixed decision threshold L_+ (L_-) determined by the prescribed accuracy [2, 4]. Here, the decision accuracies are the conditional probabilities $\alpha_+ = P(D_{\text{dec}} = 1|H_1)$ and $\alpha_- = P(D_{\text{dec}} = -1|H_2)$, and denote respectively the probability that decision $D_{\text{dec}} = 1$ ($D_{\text{dec}} = -1$) when the hypothesis H_1 (H_2) indeed is true. On the other hand, the quantity $\mathcal{P}(X_{[0,t]}|H_1)$ ($\mathcal{P}(X_{[0,t]}|H_2)$) denotes the conditional probability of observing the trajectory $X_{[0,t]}$ given hypothesis H_1 (H_2) is true. For a broad class of continuous stochastic processes, the decision thresholds ensuring symmetric accuracies $\alpha_{\pm} = \alpha$ are given by $L_{\pm} = \pm\lambda$ with $\lambda = \ln[\alpha/(1-\alpha)]$ [3]. Wald's SPRT is thus a first-passage-time problem for \mathcal{L}_t with the decision time $T_{\text{dec}} = \inf\{t \geq 0 | \mathcal{L}_t \notin (-\lambda, \lambda)\}$ given by the first exit time from the interval $(-\lambda, \lambda)$.

In thermodynamics, an enduring question is how the time irreversibility of nonequilibrium processes gives rise to entropy production in the form of e.g. heat dissipation. Consider the paradigmatic 1D drift-diffusion model (1DDM) for an overdamped Brownian particle in one dimension $\dot{X}_t = v + \sqrt{2D}\xi_t$, where X_t denotes the particle's position at time t ; v and D are the drift velocity and the diffusion constant, respectively. The quantity ξ_t is a zero-mean Gaussian white noise with autocorrelation $\langle \xi_t \xi_s \rangle = \delta(t-s)$. Suppose the task of an SPRT is to decide as soon as possible, achieving some prescribed average accuracy across trials, whether an observed stochastic path $X_{[0,t]}$ (with initial position $X_0 = 0$ and periodic boundary conditions) is produced by a 1DDM with positive speed $v > 0$ (hypothesis H_1) or instead by the time-reversed 1DDM with negative speed $v < 0$ (hypothesis H_2). The log-likelihood ratio associated with such SPRT reads $\mathcal{L}_t = \ln[\mathcal{P}(X_{[0,t]}|H_1)/\mathcal{P}(X_{[0,t]}|H_2)] = (v/D)X_t$, and coincides with the stochastic entropy production [29] associated with the stochastic trajectory $X_{[0,t]}$ [28], which for the 1DDM is proportional to the position. These relations imply that the SPRT evidence accumulation rate $\langle \dot{\mathcal{L}}_t \rangle$ equals the steady-state rate of entropy production $\Sigma \equiv v^2/D$ (in units of the Boltzmann constant) of the 1DDM, i.e., $\langle \dot{\mathcal{L}}_t \rangle = v\langle \dot{X}_t \rangle/D = \Sigma$. Furthermore, the SPRT maps in this case into the first-exit-time problem for X_t to reach any of two decision thresholds located at L and $-L$ with $L = \lambda D/v = D \ln[\alpha_{\text{SPRT}}/(1 - \alpha_{\text{SPRT}})]/v$. Consequently, the decision time is given by $T_{\text{dec}} = \inf\{t \geq 0 | X_t \notin (-L, L)\}$, whose mean value retrieved from the first-passage theory [30] reads

$$\langle T_{\text{dec}} \rangle_{\text{SPRT}} = \frac{\text{Pe}}{\Sigma} \tanh\left(\frac{\text{Pe}}{2}\right), \quad (1)$$

with the predicted accuracy set by the absorption prob-

ability $\alpha_{\text{SPRT}} = P(X_{T_{\text{dec}}} = L)$ given by

$$\alpha_{\text{SPRT}} = \frac{1}{1 + \exp(-\text{Pe})}, \quad (2)$$

where $\text{Pe} \equiv vL/D$ is the Péclet number.

Let us now consider a suboptimal decision maker [this confuses me some because there is no hint about WHAT is suboptimal about this decision maker] that collects stochastic evidence from the 1DDM and takes decisions based on a first-exit problem of \mathcal{J}_t , a functional of $X_{[0,t]}$ that may be in general different to the log-likelihood ratio (e.g. $\mathcal{J}_t = \int_0^t f(s)X_s$, with f a prescribed real function). Let $(-L_J, L_J)$ be the interval chosen such that the accuracy of the decision maker equals that of the SPRT [Eq. (2)], leading to the mean decision time $\langle T_{\text{dec}} \rangle$. Under such assumptions, the SPRT's optimality implies the relation $\langle T_{\text{dec}} \rangle \geq \langle T_{\text{dec}} \rangle_{\text{SPRT}}$, which can be generalized to a broad class of stochastic processes [3]. For the 1DDM, this relation together with Eq. (1) implies that

$$\Sigma \langle T_{\text{dec}} \rangle \geq \text{Pe} \tanh\left(\frac{\text{Pe}}{2}\right), \quad (3)$$

i.e. a tradeoff relation between dissipation (entropy production) and (mean decision) time. Equation (3) belongs to the emerging collection of quantitative predictions of thermodynamic constraints to the accuracy of nonequilibrium currents in the promising field of thermodynamic uncertainty relations (TURs) [31–34]. A fundamental lower limit to the mean decision time of the form of Eq. (3) was first conjectured for Markovian processes [28], later proved and generalized to generic nonequilibrium stationary processes [35], but never to date tested in experimental scenarios. Here we do so in a human decision-making experiment.

III. NONEQUILIBRIUM PERCEPTUAL EXPERIMENT AT WORK

In a behavioral experiment, we tasked 21 healthy human participants with deciding the net direction of a stochastic visual stimulus moving with a given drift velocity and a given diffusion coefficient. See Fig. 1A for a sketch of the experiment, and Supplementary Sec. S1 for additional information about the participants. We generated many trials of movies of a dark gray disk displayed on a computer screen on a light gray background. In each trial, the trajectory of the disk's center of mass (X_t, Y_t) was obtained by simulating the nonequilibrium dynamics of an overdamped Brownian particle in two dimensions (see Materials and Methods section VII). The corresponding dynamics is set by the Langevin equation $\dot{X}_t = Hv + \sqrt{2D}\xi_t$, $\dot{Y}_t = \sqrt{2D}\eta_t$. Here, $v > 0$ is the drift velocity along the x -axis, and $D > 0$ is the diffusion coefficient, which we take equal along the x and y axes. The dichotomous random variable $H = \{1, -1\}$ sets the left/right direction of the drift, and in each

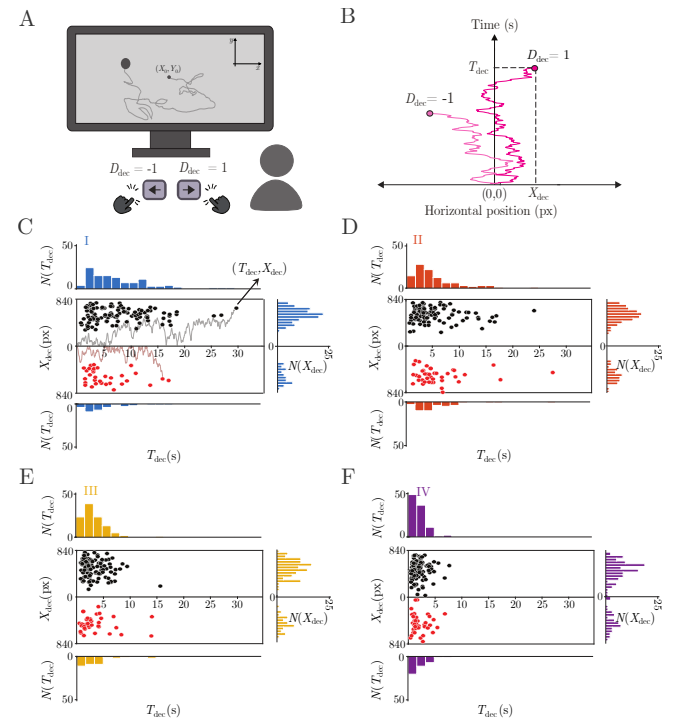


FIG. 1: **Sketch of the experimental setup and data collection.** (A) Twenty one human participants were instructed to judge the net motion direction (left versus right) of a moving disk displayed on a computer screen by pressing the right (left) arrow key on a keyboard. The snapshots of the disk's motion are generated from stochastic simulations described in the main text. (B) Example traces of x -position over time shown in fuchsia. For each trial, we collect the decision time (T_{dec} , in seconds), the position of the disk along the x -axis (X_{dec}) and y -axis (Y_{dec} , not illustrated here), in pixels, and the decision outcome ($D_{\text{dec}} = 1$ for right, or $D_{\text{dec}} = -1$ for left). We also store the trajectories of the disk up to the decision time (gray line in panel A). (C-F) Experimental data collected from a typical participant across the four experimental conditions, each characterized by a selected value of v and D . For each condition, the plots in the middle show X_{dec} as a function of T_{dec} . The black and red dots indicate correct and incorrect decisions, respectively. Histograms are obtained from empirical counts of T_{dec} for correct (top) and incorrect decisions (bottom) and for X_{dec} for correct (top) and incorrect (bottom) decisions. In C-F, we pool the statistics of trials with positive and negative drift for both correct and incorrect decisions.

trial is randomly set to -1 or 1 with equal probability. The quantities ξ_t and η_t are independent Gaussian white noises, each with zero mean and satisfying correlations $\langle \xi_t \xi_s \rangle = \langle \eta_t \eta_s \rangle = \delta(t-s)$, $\langle \xi_t \eta_s \rangle = 0$ for all t, s . Such simulations mimic the fluctuating motion of an overdamped Brownian particle dragged at a constant net speed v in a Newtonian fluid with viscosity $\gamma = k_B T/D$, where k_B is Boltzmann's constant and T is the temperature of the fluid. Thus, our experimental setup serves as a minimal yet flexible platform to study human perception of nonequilibria.

The task of the participants was to judge, as rapidly as possible, the net direction of the disk along the x -axis (“rightwards” or “leftwards”) by pressing the arrow keys of a computer keyboard. After a 20-trial training period with subject responses and feedback (correct/incorrect), experimental data were collected. See Supplementary Sec. S1 for further details about the experiments. No knowledge of the underlying dynamics of the disk was provided to the participants, not even the fact that the trajectory arose from physical equations of motion. Participants reached decisions about whether the drift of the disk was rightward ($D_{\text{dec}} = 1$) or leftward ($D_{\text{dec}} = -1$) (Fig. 1A) at stochastic times T_{dec} . For each trial and each subject, we recorded relevant decision-making quantities (see Fig. 1B): (i) the true hypothesis (ground truth), i.e., the actual direction of the net drift $H = \{1, -1\}$; (ii) the decision outcome $D_{\text{dec}} = \{1, -1\}$; (iii) the decision time T_{dec} ; (iv) the position of the disk along the x -axis of the screen at the decision time, $X_{\text{dec}} = X(t = T_{\text{dec}})$; and (v) the full stochastic trajectory $X_{[0, T_{\text{dec}}]}$ of the disk up to T_{dec} . From now on, we will refer to X_{dec} as the *decision threshold* [49].

IV. DATA ANALYSIS

To facilitate the statistical analysis of our experiment, we presented to each participant the same set of movies of stochastic trajectories, but the presentation order of distinct movies was randomized across participants. We explored four experimental conditions (denoted I, II, III, and IV), each comprising different sets of stimuli defined by the drift velocity v and the diffusivity D . The entropy production rate $\Sigma = v^2/D$ monotonically increases from condition I to condition IV, while the ratio v/D is kept same across conditions (see Table I in Methods for the values of v and D in each condition). See Fig. 1C for a typical trajectory of X -position of the disk as a function of time until decision time [50]. Figures 1C–F display the data collected from one participant in the four experimental conditions, each comprising 150 independent trials.

We first focus on the decision outcome D_{dec} , the decision time T_{dec} , and the decision threshold X_{dec} . We observe from Figs. 1C–F that the participant made more correct decisions ($D_{\text{dec}} = H$, black circles) than incorrect decisions ($D_{\text{dec}} \neq H$, red circles), with an accuracy of $\sim 70\%$ for all the experimental conditions (see below). The statistics of T_{dec} (top and bottom histograms in Figs. 1C–F) varied significantly across conditions; the histograms of T_{dec} peak towards smaller values and get sharper with increasing Σ , suggesting a reduction of the mean $\langle T_{\text{dec}} \rangle$ of decision times. Contrarily, for the decision thresholds the mean $\langle X_{\text{dec}} \rangle$ does not change significantly with increasing Σ (see histograms on the right in Figs. 1C–F). We observe similar behaviour of $\langle T_{\text{dec}} \rangle$ and $\langle X_{\text{dec}} \rangle$ on the ensemble level of all participants (Fig. 2). This observation motivates us to study whether Wald’s

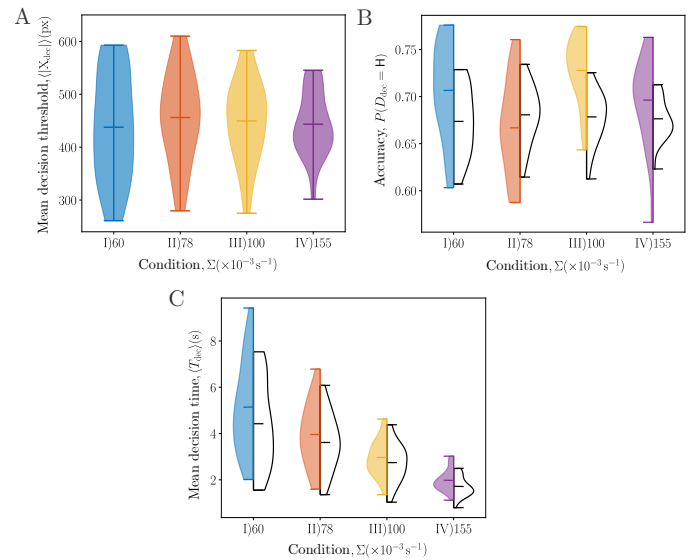


FIG. 2: **Statistics of the participants’ mean values of decision-making quantities as a function of experimental conditions labeled by entropy production rate Σ .** (A) Distribution of mean decision threshold $\langle |X_{\text{dec}}| \rangle$, (B) accuracy $P(D_{\text{dec}} = H)$, and (C) mean decision time $\langle T_{\text{dec}} \rangle$. Experimental (filled) violin plots are obtained by collecting the statistics of each participant’s mean decision threshold amplitude (A), accuracy (B), and mean decision time (C). Plots were obtained by averaging over all trials for every participant. The empty violin plots in (B, C) illustrate the distribution of the theoretical predictions from Wald’s SPRT with thresholds set at $\pm \langle |X_{\text{dec}}| \rangle$ obtained from experiment for each participant. Central horizontal lines show the respective means. SPRT predictions of mean decision time and accuracy were obtained by plugging Péclet number and entropy production rate in Eqs. (1) and (2), respectively.

SPRT, which assumes fixed decision thresholds, is suitable for studying perceptual decision-making of nonequilibrium fluctuations.

To inspect whether there exist generic principles that constraint the decision-making process at the ensemble level, we focus on the mean decision threshold, mean accuracy, and mean decision time, all of them averaged over all trials and over all participants (see Fig. 2). For such analysis, we characterize each condition (v, D) by its entropy production rate $\Sigma = v^2/D$, which in this case is given by the average power dissipated by the friction force. Interestingly, we find an Σ –independent behaviour for the mean decision threshold $\langle X_{\text{dec}} \rangle$ (Fig. 2A). An analogous behaviour is found in subjects’ mean accuracy (Fig. 2B), measured by the fraction of times a correct decision is taken, which does not vary across conditions and is thus independent on the entropy production rate. On the other hand, the mean decision time $\langle T_{\text{dec}} \rangle$ averaged over all participants is inversely proportional to the entropy production rate (Fig. 2C), as predicted by previous theoretical work [28]: it takes less time on average to decide on the direction of time’s arrow when

observing a process that is far from equilibrium; here, this corresponds to the case where the disk's motion is highly irreversible. The contrasting behaviour of $\langle X_{\text{dec}} \rangle$ and $\langle T_{\text{dec}} \rangle$ suggests a dissociation between the time of the decision and the spatial position of the disk at the moment of the decision (see Supplementary Sec. S2 for the statistical tests of linear mixed effects modeling and ANOVA).

We now test whether the decision-making statistics averaged over all participants can be faithfully described by a theoretical model. The results in Fig. 2 suggest that Wald's SPRT may describe at least qualitatively our data at the ensemble level. In particular, we consider Wald's SPRT with symmetric error probabilities and symmetric thresholds located at $\pm L$, with $L = \langle |X_{\text{dec}}| \rangle$ set at the ensemble-average of the observed absolute value of the decision thresholds. We compare in Figs. 2B and 2C the theoretical predictions for the SPRT's mean accuracy [Eq. (2)] and mean decision time [Eq. (1)] with the experimental values, respectively. The mean accuracy can be well described by the SPRT, which also predicts similar values across conditions. This follows from the fact that the Péclet number $\text{Pe} = vL/D$ (and thus α_{SPRT} in Eq. (2)) remains effectively the same across conditions. Similarly, the experimental mean decision times may also be described by the SPRT in all experimental conditions (See Supplementary Sec. S3 for further statistical analyses). Additionally, note that for all conditions the experimental mean decision times are greater than the optimal time predicted by the SPRT.

Strikingly, we further verify SPRT's optimality at the individual participant level, by inspecting the statistics of each participant in each of the tested conditions. Figure 3 shows that the mean decision time of each participant in each condition fulfills the thermodynamic uncertainty relation conjectured given by Eq. (3). Here, the fundamental lower bound from the right-hand side of Eq. (3) is set by using an effective Péclet number $\text{Pe} = v\langle |X_{\text{dec}}| \rangle/D$ associated with the statistics of each participant in each trial.

V. EVIDENCE INTEGRATION MODEL

In sum, the behavior of human participants is consistent with the decisions being based on entropy production rate $\Sigma = v^2/D$, yet choices were longer in time than that predicted by SPRT given the observed accuracy level. Thus, human participants are suboptimal and we now explore how evidence might in fact be integrated, if not optimal. The fact that the experimental results supporting the fundamental bound Eq. (3) through an inverse proportionality relation between the mean decision time and the entropy production motivates us to search for a new theoretical model to tighten the observed quantitative difference with the experimental results. From a cognitive neuroscientific viewpoint, the evidence accumulation process entails two aspects:

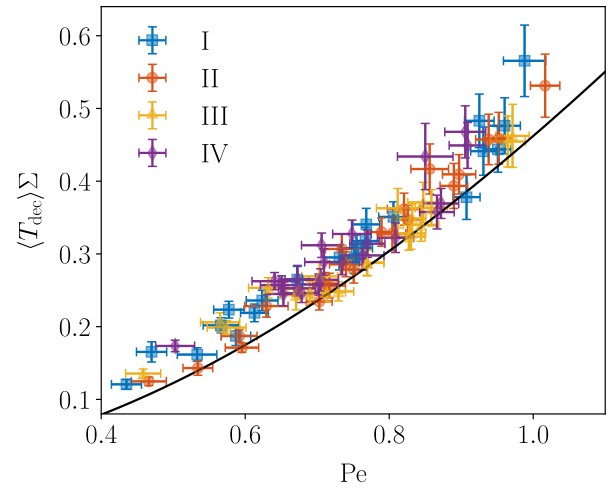


FIG. 3: **Experimental test of the dissipation-time thermodynamic uncertainty relation Eq. (3).** Mean decision time (times the rate of dissipation $\Sigma = v^2/D$) as a function of the participants' effective Péclet number. Each symbol is obtained from the statistics of a single participant, and different shapes and colors are used to denote different conditions. The effective Péclet number for each participant is estimated from the mean absolute value of the participant's decision threshold in each condition as $\text{Pe} = v\langle |X_{\text{dec}}| \rangle/D$. The black line shows the fundamental lower bound given by $\text{Pe} \tanh(\text{Pe}/2)$.

retaining a recollection of previously gathered evidence and incorporating new evidence into the existing memory [24]. Wald's SPRT only assumes that participants accumulate X_t as evidence, but it does not attempt to explain how the brain accumulates information before making a decision. Moreover, Wald's SPRT fails to account for the variability observed in the decision-making statistics gathered for each participant. When we focus on the trial-by-trial progress of the decision thresholds for the participants, we find a broad decision-threshold distribution across the experimental conditions (e.g., see histograms of decision thresholds in Figs. 1C–F for one participant). Notably, the observed variance in the decision thresholds is not predicted by Wald's SPRT with log-likelihood ratio $\mathcal{L}_t = \ln[\mathcal{P}(X_{[0,t]}|H_1)/\mathcal{P}(X_{[0,t]}|H_2)]$, which describes X –thresholds as fixed. Our data also reveals that individual movie choices covary among subjects, which reveals the key role of specific features in individual stimuli.

To build a more comprehensive model that incorporates both thermodynamic insights as well as the limited capacity of human observers, we introduce the Evidence Integration Model (EIM) for decision making. In this model, the accumulation of evidence is given by an accumulator W_t that is a functional of $X_{[0,t]}$ defined by

$$W_t \equiv \frac{1}{\tau_m} \int_0^t ds e^{-s/\tau_m} X_{t-s}, \quad (4)$$

where τ_m is a parameter denoted *memory relaxation*

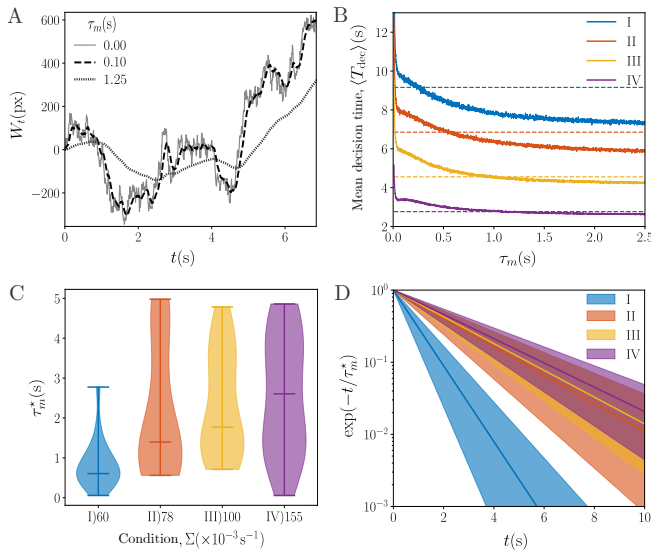


FIG. 4: **Evidence Integration Model (EIM): sample trajectories and parameter inference.** (A) Sample trajectories for the decision accumulator W_t associated with a given trajectory of the position X_t for different memory relaxation times τ_m . Note that for $\tau_m = 0$, one gets $W_t = X_t$ (gray solid line). (B) Inference of the optimal memory relaxation time τ_m^* for one participant in the four conditions: experimental mean decision time (horizontal dashed lines), and mean escape time of W_t from the interval $(-L_W, L_W)$ extracted from numerical simulations (solid lines) as a function of τ_m . Here $L_W = \langle |W_{T_{\text{dec}}}|\rangle$ is determined from experimental trajectories $X_{[0, T_{\text{dec}}]}$ (see Fig. 1). For each condition and each participant, we identify τ_m^* as the value of τ_m yielding the minimal difference between the experimental and simulated mean decision times. (C) Distribution of the inferred τ_m^* for all participants in each condition. Central horizontal lines are set at the respective medians. See Tab. S6 in Supplementary Sec. S4. (D) Inferred exponential memory kernel (see Eq. (4)) associated with τ_m^* (solid lines) averaged over all participants in each condition. The shaded area spans over the standard error of the mean of τ_m^* averaged over all participants.

time. Thus, the evidence, accumulated to make a decision and represented by the accumulator W_t , is characterized by the exponentially weighted area swept by the stimulus X_t in the (X, t) domain. The constraint of limited memory might be one feature that renders humans as suboptimal. Note that the stimulus in Eq. (4) is read backward in time, giving exponentially less weight e^{-s/τ_m} to the past evidence X_{t-s} with respect to the evidence at time t . From Eq. (4) one may write $\tau_m \dot{W}_t = -W_t + X_t$. For the stimulus X_t given by the stochastic process $\dot{X}_t = Hv + \sqrt{2D}\xi_t$, the accumulator W_t obeys an underdamped Langevin equation $\tau_m \ddot{W}_t = -\dot{W}_t + Hv + \sqrt{2D}\xi_t$, in which τ_m acts as an effective inertial relaxation time. Figure 4A shows typical trajectories of the accumulator W_t associated with the stochastic stimulus X_t for different values of τ_m . The short memory limit $\tau_m \rightarrow 0$ corresponds to the overdamped limit $W_t \rightarrow X_t$, whereas for

larger τ_m underdamped dynamics are generated, making the accumulator a smoothed version of the stimulus. To fully characterize the model, we establish the *EIM decision criterion* to be given by the first exit of W_t through either boundary of a symmetric interval $(-L_W, L_W)$: a decision $D_{\text{dec}} = +1$ if W_t first reaches L_W before reaching $-L_W$, and vice versa for a decision $D_{\text{dec}} = -1$. This results in a decision-making model with two free parameters τ_m and L_W , both to be fitted from the experimental data.

We hypothesize that each participant builds for each condition intrinsic values for the memory relaxation time and decision threshold, which we denote as τ_m^* and L_W^* , respectively. To infer τ_m^* for a participant in a given condition, we explore a range of possible values of τ_m (see Fig. 4) determined empirically. For each value of τ_m , evaluating Eq. (4) along the trajectories $X_{[0, T_{\text{dec}}]}$ extracted from the experiment, we obtain the decision threshold $L_W = \langle |W_{T_{\text{dec}}}|\rangle = \langle |W_{T_{\text{dec}}}|\rangle$ as the average of the absolute value of the decision accumulator at the decision time. After this step, we have a collection of parameter pairs $\{(\tau_m, L_W)\}$. For each pair (τ_m, L_W) , we employ the EIM criterion to obtain from numerical simulations the mean exit time of W_t from $(-L_W, L_W)$. The intrinsic memory time τ_m^* is identified as the particular value of τ_m , for which the mean exit time obtained from simulations (solid lines in Fig. 4B) yields the closest value to the experimentally observed mean decision time (dashed lines in Fig. 4B). The corresponding value of L_W is chosen to be L_W^* . Importantly, the empirical distribution of W_{dec} associated with the values τ_m^* and L_W^* is significantly narrower than the one of X_{dec} (c.f. Figs. 1C–F and Fig. S3), signifying that the EIM decision-making strategy (responding when W exits an interval) constitutes an improved model to account for real data. Interestingly, the median of τ_m^* over all participants increases with the entropy production rate Σ , indicating that participants deploy a longer-time constant memory trace when taking acting on movies with a higher degree of nonequilibrium (see Figs. 4C,D).

Customarily, to fully validate decision-making models, it is advisable to pursue a trial-by-trial statistical analysis which may shed light on the underlying mechanisms of dynamic decision-making in noisy environments [20, 22–24]. The model, ideally, tracks the variability expressed by actual subjects. We test the EIM by quantifying the quality of its prediction of decision-making statistics at trial-by-trial resolution (see Fig. 5). To this aim, Figs. 5A–B show joint histograms of the predicted and the experimental decision times collected from all trials of all participants, under all conditions, for the SPRT (Fig. 5A) and EIM (Fig. 5B). See Supplementary Sec. S6 for additional analysis related with the robustness of decision thresholds used to predict decision times. We proceed similarly for the joint histograms of decision thresholds in Figs. 5C–D comparing experimental outputs with predictions from the SPRT (Fig. 5C) and EIM (Fig. 5D). Notably, the decision-times statistics from the experi-

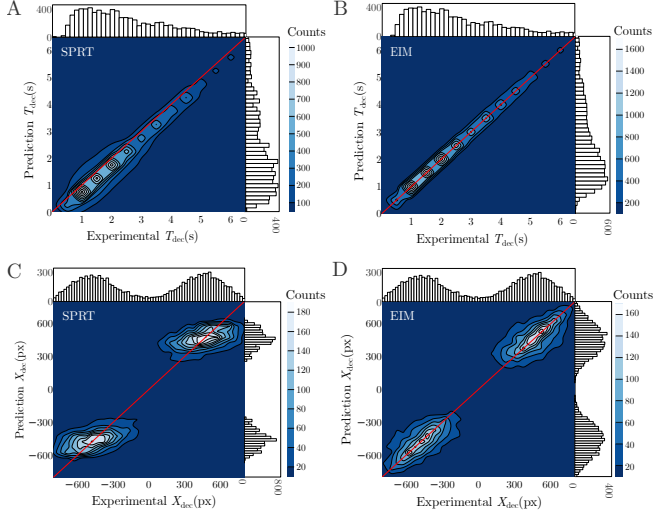


FIG. 5: Comparison of decision-making models (SPRT and EIM) with experimental decision times and decision thresholds. (A-B) Joint histogram of the trial-by-trial experimental decision time T_{dec} for all participants and conditions, and the numerical predictions of T_{dec} by Wald's SPRT (A) and the EIM (B). (C-D) Joint histogram of the trial-by-trial experimental decision threshold X_{dec} for all participants and conditions, and the numerical predictions of X_{dec} by Wald's SPRT (C) and the EIM (D). The red lines have slope one, representing the region with perfect agreement between the experimental output and model predictions.

ment are statistically indistinguishable from the predictions of the EIM, providing predictions significantly more accurate than the SPRT, with the latter yielding a systematic trend of predicting faster decisions (below the diagonal) compared to the experimental observations (see Supplementary Sec. S4 for statistical tests). Interestingly, we observe the same phenomenon for the decision thresholds X_{dec} , for which the EIM provides an even more significant improvement in predicting the experimental outcome compared to the SPRT (see Supplementary Sec. S2). Note that we observe that the distribution of X_{dec} associated with the SPRT shows fluctuations despite such decisions being taken when X_t crosses well-defined thresholds. See Supplementary Sec. S5 for further analysis on X_{dec} variance. In Fig. 5C, the horizontal elongation of the joint predicted versus observed X_{dec} indicates that the SPRT prediction was not sensitive to trial-to-trial "noise" in the disk trajectory, while the EIM (Fig. 5D) was sensitive. Our findings in this section lend further credence to the EIM as a mechanism in which the brain accumulates evidence before making a binary decision about nonequilibrium fluctuations.

VI. DISCUSSION

Our work shows that the decision statistics of human perceptual binary decision making of nonequilibrium

phenomena is constrained by a fundamental thermodynamic trade-off between decision time, accuracy and entropy production. Through a multidisciplinary approach combining stochastic thermodynamics and cognitive neuroscience, our experiment quantifies the deviation from humans decisions from optimality. Such measurable deviation from SPRT's optimality is small yet sufficient to develop EIM with a strong predictive power on a trial-by-trial basis, revealing insights into the cognitive strategies that support efficient decision-making. In particular, our research suggests that humans adapt their memory integration window to the rate of dissipation of the observed phenomenon, favouring memory over momentary evidence for effective decisions in scenarios where stimuli are far from equilibrium. This finding highlights the importance of using stimuli produced from simulations of statistical-physics models in perceptual decision tasks. Through the usage of controllable (yet stochastic) nonequilibrium physical stimuli in perceptual experiments our work establishes a promising robust platform to strengthen the connections between specific patterns in stimuli noise fluctuations (e.g., entropy production rate) and the inter-trial variability of decision outcome (e.g., variance in X_{dec}) through specific decision mechanisms (e.g., adapting integration windows). Adapting the time scale of integration as opposed to a perfect integration mechanism has been suggested as a strategy to overcome the volatility of the signal by reducing the noise in order to avoid false alarms [36–38]. We thus expect our work will inspire further investigation in the multidisciplinary domain at the frontier between nonequilibrium statistical physics and neuroscience [39, 40].

An exhaustive exploration of the neural dynamics governing perceptual decision-making during non-equilibrium fluctuations provides fruitful opportunities for future research. For instance, NMDA-mediated synapses have been highlighted as potential modulators of integration time windows in the brain [41–43]. In addition to the neurobiological mechanisms, the dynamics of macroscale brain activity for perceptual decision making of non-equilibrium fluctuations is also open for future inquiry. The best insights so far have revealed, using brain imaging methods, that human and primate brain dynamics exhibits speed-accuracy trade-offs [27] and a measurable degree of time irreversibility [40] that depends on the type of cognitive tasks [40], consciousness levels [44, 45], and pathology in the brain [46, 47]. These perspectives are promising not only advancing our understanding of human cognition but also lighting the broader principles governing complex systems taking swift and accurate decisions in a changing world.

VII. MATERIALS AND METHODS

Main experiment. The experiment comprises four experimental conditions, each characterized by prescribed values of the drift velocity and diffusivity (see Ta-

ble I). The parameter values are chosen such that across

Condition	v (px/s)	D (px 2 /s)	Σ (s $^{-1}$)
I	36	21600	0.060
II	47	28200	0.078
III	60	36000	0.100
IV	93	55800	0.155

TABLE I: Parameter values for the drift velocity v , diffusivity D , and entropy production rate $\Sigma = v^2/D$ used in the experimental conditions (I, II, III, and IV).

conditions, the entropy production rate v^2/D varies, yet the ratio $v/D \simeq 1.67 \times 10^{-3}$ px $^{-1}$ is kept the same across conditions. For each condition and each participant, we have carried out 3 blocks of 50 trials each, summing up to 12 blocks of 50 trials, i.e., 600 trials in total. All participants are displayed with the same set of 600 trial movies. However, the order of the blocks and the trials within a block are randomized for each participant. Participants are asked to sit in a room with dim light in front of the lab computer equipped with a 2233RZ series business monitor with a spatial resolution of [1680 px \times 1050 px] and temporal resolution of 120 Hz. Throughout the experiments, a chin rest is used to constrain head movements and fix the head position at a distance of 57 cm from the computer screen.

The stimuli (a disk with a diameter of 2° degrees of visual angle) are located in the center of the screen in the beginning of the trials. Each trajectory of the disk is generated by performing an Euler numerical integration of the Langevin equation $\dot{X}_t = Hv + \sqrt{2D}\xi_t$ and $\dot{Y}_t = \sqrt{2D}\eta_t$ with $H = \pm 1$, a binary random variable sampled with equal probability. The discrete time step in numerical simulations is chosen to be the inverse of the screen's temporal resolution.

Data analysis. All data analyses are performed in R, Python, and MATLAB 2020. Prior to the analyses, we remove from the dataset the missed trials ($\sim 5\%$) in which participants have not taken a decision before the disk reaches the screen edge. We have used the lmer program from the lme4 package [48] for the linear mixed effects modeling.

VIII. ACKNOWLEDGEMENTS

MED acknowledges financial support from Human Frontier Science Program, project RGP0017/2021, European Union Horizon 2020 MSCA Programme NeuTouch under Grant Agreement No 813713, Italian Ministry PRIN 2022 Contract 20224FWF2J.

DB acknowledges financial support from the European Research Council–ERC (Grant Agreement No 682117, BiT-ERC-2015-CoG), the Italian Ministry of University and Research under the call FARE (project ID: R16X32NALR) and under the call PRIN2022 (project ID: CCPJ3J).

ER acknowledges financial support from PNRR MUR project PE0000023-NQSTI.

We thank Antonio Celani, Stefano Ruffo, and Jin Wang for valuable discussions.

Supplemental Material

S1. EXPERIMENTAL DETAILS

Participants. Twenty one right-handed participants, aged between 23 and 59, with normal or corrected-to-normal vision were recruited ($N_{Female} = 12$, $M = 30.76$, $SD = 8.8$) on a voluntary basis for the main experiment. The participants are tested for approximately 1 to 1.5 hours depending on their own pace. All the participants are tested in the laboratory of International School for Advanced Studies, SISSA, Trieste. Prior to the experiment, the written consent form approved by the Ethics Committee of SISSA is given and obtained from the participants. At the end of the experiment, all participants are provided with a debriefing session.

Procedure and data collection. Prior to the experiment, participants undergo a training session to familiarize them to the task. The experiment is designed as a two-alternative forced choice task. As soon as the trial starts, participants are required to report the direction of the disk by pressing the right (left) arrow key corresponding to the right (left) direction before the disk reaches any of the edges of the screen. After each trial the participants receive immediate feedback of three possible outcomes that they could get from their response together with an accumulating score: (i) correct responses (+35 points), (ii) incorrect responses (-20 points), and (iii) missed trials (-50 points), accompanying with a sound and color of the feedback text in accordance with the outcome. After receiving feedback, participants are asked to press the space bar to start the next trial in their own time (Fig. S1). All the displays and the data collection were coded by using MATLAB software, and Psychophysics Toolbox Version 3 (PTB-3).

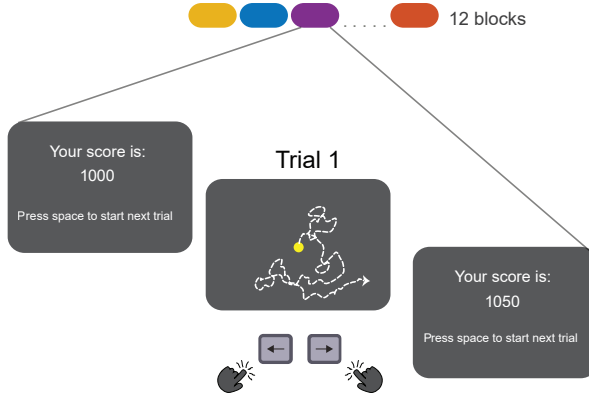


FIG. S1: **Schematics of visual displays in the experiment.** Each of the 12 blocks consists of trials from the same condition. For each condition, the trials are shown in 3 blocks. In the beginning of each block, participants start with 1000 points. The score is accumulated within each block as participants give correct, incorrect, or missed responses, and in the next block participants start with 1000 points afresh.

Control experiment. Among the participants of the main experiment, 9 individuals have also participated in the control experiment. For the control experiment, the lab computer has a BenQ ZOWIE XL2731 Monitor, with a spatial resolution of [1920 px \times 1080 px], and a temporal resolution of 144 Hz. The temporal resolution in the motor implementation experiment is set the same as the main experiment. The control experiment comprises three parts with varying parameters of the stimuli. For all the parts, participants are instructed to press the right (left) key as soon as the disk reaches the right (left) red line visible to the participants throughout the trials. Note that here the participants do not make decisions on the direction of the disk's motion. Instead, they only need to react as soon as the disk reaches either of the visible lines. Therefore, we refer to the control experiment as decision-free response task. All parts of the control experiment consist of 160 trials separated into 4 blocks. First part ('no diffusion' version) has stimuli with a velocity of 480 px/s. In the second part of the experiment ('Y-axis diffusion' version), in addition to the drift there is also a diffusivity component in the Y-axis of 21600 px²/s. Third part ('original parameter' version) has stimuli with the same velocity and diffusivity as the main experiment. The order of these parts are randomized within participants. In the control experiment, participants do not receive any feedback.

S2. LINEAR MIXED EFFECTS STATISTICAL MODELING

In this section we provide additional details about statistical tests that we carried to support the data analyses presented in the Main Text.

Decision thresholds. We consider $\langle X_{\text{dec}} \rangle$ data as a function of experimental conditions as fixed effects, and participant identities as random effects to obtain model X_{dec}

$$\text{model } X_{\text{dec}} \leftarrow \langle X_{\text{dec}} \rangle \sim \text{Experimental condition} + (1 | \text{participant_id}) \quad (\text{S1})$$

The ANOVA test performed on the obtained model X_{dec} , reveals no significant effect (see Table S1). The mean decision thresholds are kept fixed under different experimental conditions, meaning the participants do not modulate their mean threshold with different conditions.

	Sum Sq	Mean Sq	NumDF	DenDF	F value	Pr(>F)
condition	8878.1	2959.4	3	60	2.4023	0.07644

Signif. codes: 0 ‘***’ 0.001 ‘**’ 0.01 ‘*’ 0.05 ‘.’ 0.1 ‘ ’ 1

TABLE S1: Type III Analysis of Variance Table with Satterthwaite’s method (model X_{dec}).

Accuracies. Similar to the decision thresholds analysis, we obtain the model accuracy from the accuracy data by considering experimental conditions as fixed effects and participant identities as random effects, and using

$$\text{model accuracy} \leftarrow \text{accuracy} \sim \text{Experimental conditions} + (1 | \text{participant_id}). \quad (\text{S2})$$

The ANOVA test performed on the obtained model accuracy reveals a statistically significant effect of the experimental conditions over accuracy with $F_{3,60} = 5.52$ and $p < 0.001$ (see Table S2). Post-hoc analysis reveals that only experimental condition II is significantly different compared to the condition I with $p < 0.001$ (see Table S3).

	Sum Sq	Mean Sq	NumDF	DenDF	F value	Pr(>F)
condition	0.041048	0.013683	3	60	5.5243	0.002041 **

Signif. codes: 0 ‘***’ 0.001 ‘**’ 0.01 ‘*’ 0.05 ‘.’ 0.1 ‘ ’ 1

TABLE S2: Type III Analysis of Variance Table with Satterthwaite’s method (model accuracy).

	Estimate	Std. Error	df	t value	Pr(> t)
(Intercept)	0.70211	0.01310	61.81327	53.579	$< 2 \times 10^{-16}$ ***
condition2	-0.04171	0.01536	60	-2.715	0.00863 **
conditions3	0.01822	0.01536	60	1.186	0.24018
condition4	-0.01729	0.01536	60	-1.126	0.26465

Signif. codes: 0 ‘***’ 0.001 ‘**’ 0.01 ‘*’ 0.05 ‘.’ 0.1 ‘ ’ 1

TABLE S3: Fixed effects (model accuracy).

Decision times. We consider $\log(T_{\text{dec}})$ data as a function of experimental conditions as fixed effects, and participant and trial identities as random effects to obtain model T_{dec}

$$\text{model } T_{\text{dec}} \leftarrow \log(T_{\text{dec}}) \sim \text{Experimental conditions} + (1 | \text{participant_id}) + (1 | \text{trial_id}). \quad (\text{S3})$$

This suggests that T_{dec} may be modeled by the experimental conditions when the variance due to participant and trial identities is taken aside. Furthermore, with the obtained model T_{dec} we perform the ANOVA test, which reveals a statistically significant effect of the experimental conditions over T_{dec} with $F_{3,11826} = 914.83$ and $p < 0.001$ (see Table S4).

Post-hoc analysis reveals that all experimental conditions are significantly different compared to the condition I with $p < 0.001$ (see Table S5).

	Sum Sq	Mean Sq	NumDF	DenDF	F value	Pr(>F)
condition	1176.1	392.05	3	11826	914.83	$< 2.2 \times 10^{-16}$ ***
Signif. codes: 0 ‘***’ 0.001 ‘**’ 0.01 ‘*’ 0.05 ‘.’ 0.1 ‘ ’ 1						

TABLE S4: Type III Analysis of Variance Table with Satterthwaite’s method (model T_{dec}).

	Estimate	Std. Error	df	t value	Pr(> t)
(Intercept)	1.311	6.241×10^{-2}	2.116×10	21.01	$< 1.18 \times 10^{-15}$ ***
condition2	-2.271×10^{-1}	1.678×10^{-2}	1.182×10^4	-13.54	$< 2 \times 10^{-16}$ ***
condition3	-4.400×10^{-1}	1.687×10^{-2}	1.183×10^4	-26.08	$< 2 \times 10^{-16}$ ***
condition4	-8.558×10^{-1}	1.701×10^{-2}	1.183×10^4	-50.32	$< 2 \times 10^{-16}$ ***

Signif. codes: 0 ‘***’ 0.001 ‘**’ 0.01 ‘*’ 0.05 ‘.’ 0.1 ‘ ’ 1

TABLE S5: Fixed effects (model T_{dec}).

S3. CHI-SQUARE ANALYSIS FOR WALD’S SPRT

Accuracies. Chi-square (χ^2) goodness of fit tests are performed for each condition to determine to what extent the distribution of accuracies predicted from SPRT is close to the distribution of the experimental accuracy data. The χ^2_c of accuracy for condition c is computed using

$$\chi^2_c = \frac{(\langle \alpha_{\text{SPRT}}^{p,c} \rangle_p - \langle \alpha^{p,c} \rangle_p)^2}{\text{std}(\alpha_{\text{SPRT}}^{p,c})_p^2 + \text{std}(\alpha^{p,c})_p^2}, \quad (\text{S4})$$

where $\alpha^{p,c}$ and $\alpha_{\text{SPRT}}^{p,c}$ denote the accuracies from the experiment and the predictions of SPRT for participant p in condition c , respectively. Here, the symbols $\langle \cdot \rangle_p$ and $\text{std}(\cdot)_p$ represent the average and standard deviation with respect to the participants, respectively. The corresponding χ_c values for conditions I, II, III, and IV are obtained to be 1.94, 1.25, 0.88, and 0.75, respectively. These values indicate the standard deviation of the difference of theoretical and experimental data of accuracy in comparison to a distribution with zero mean.

Decision times. Chi-square (χ^2) goodness of fit tests are also performed for each condition and each participant to determine to what extent the distribution of decision times predicted from SPRT is close to the distribution of the experimental decision times data. The $\chi^2_{p,c}$ of decision times for participant p in condition c is computed using

$$\chi^2_{p,c} = \left(\frac{\langle T_{\text{dec}} \rangle_{\text{SPRT}}^{p,c} - \langle T_{\text{dec}}^{p,c,i} \rangle_i}{\text{std}(T_{\text{dec}}^{p,c,i})_i} \right)^2, \quad (\text{S5})$$

where $T_{\text{dec}}^{p,c,i}$ denotes the experimental decision times for participant p in condition c and trial i , and $\langle T_{\text{dec}} \rangle_{\text{SPRT}}^{p,c}$ denotes the SPRT predictions of mean decision times for participant p in condition c . Here, the symbols $\langle \cdot \rangle_i$ and $\text{std}(\cdot)_i$ represent the average and standard deviation with respect to the trials. The obtained $\chi^2_{p,c}$ values for each condition are summed across participants, and then a $\chi_c = \sqrt{\sum_p \chi^2_{p,c}}$ is calculated. We thus obtain χ_c values 1.16, 0.62, 0.83, and 1.19 for conditions I, II, III, and IV, respectively. These values indicate the standard deviation of the difference between the distributions of experimental decision times and the SPRT’s predictions.

S4. EVIDENCE INTEGRATION MODEL

Discrete-time interpretation. One may rewrite Eq. (4) in discrete times with time steps Δt as

$$W_{t+\Delta t} = e^{-\Delta t/\tau_m} W_t + \frac{\Delta t}{\tau_m} X_{t+\Delta t}. \quad (\text{S6})$$

The first term on the right-hand side of Eq. (S6) denotes the prior knowledge W_t accumulated until time t and captures the memory of the evidence accrued so far. The exponential factor $e^{-\Delta t/\tau_m}$ in this term acts as a weight, suggesting that the significance of the memory becomes higher as the relaxation time τ_m increases. On the other hand, the second term on the right-hand side of Eq. (S6) acts as the instantaneous evidence and adds the latest information to the

existing memory in terms of the present position of the disk. The factor $(\Delta t/\tau_m)$ in this term suggests that the latest instantaneous evidence for large relaxation time τ_m becomes less significant compared to the previously accumulated evidence. Thus, by construction, the decision accumulator W_t , depending on τ_m , automatically captures a trade-off between the memory and the instantaneous evidence uptake. Higher reliance on memory for stimuli further from equilibrium may be a strategy used by participants in order to capture evidence history more holistically and thus reduce the noise of the input in memory.

Intrinsic memory relaxation time. Here, we check the robustness of our hypothesis (made in Sec. V) that each participant builds for each condition an intrinsic τ_m^* . To this end, we randomly split the trial-by-trial data for each participant into two segments of equal size. We then identify for each segment the corresponding memory relaxation times denoted by τ_m^* and τ_m^\diamond using the same procedure mentioned in Sec. V of the main text. Figure S2 displays for each condition the scatter plots of τ_m^* and τ_m^\diamond , in which each data point represents a participant. From the figure, we observe that most of the points lie on the diagonal, indicating the fact that $\tau_m^* \simeq \tau_m^\diamond$. The similarity of the values from the two independent segments suggests that there exists one intrinsic memory relaxation time associated with each participant in each condition. We also show the global mean and median of τ_m^* considering all participants in each condition in Table S6.

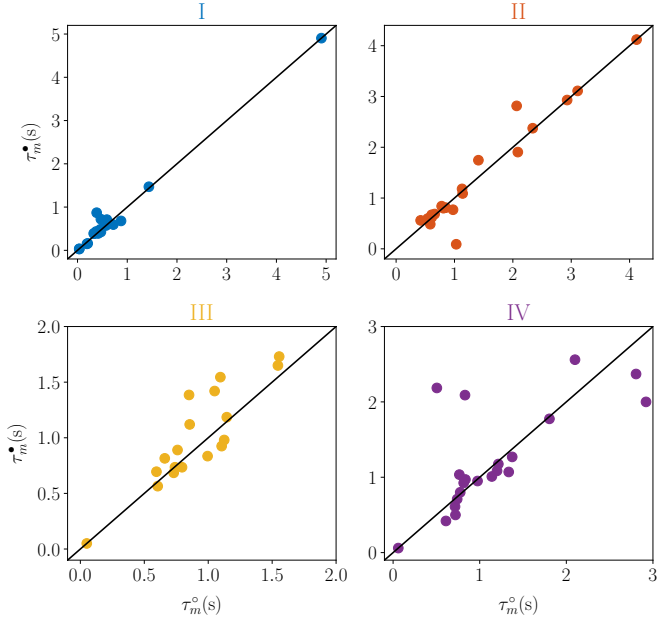


FIG. S2: **Cross validation of the memory relaxation time.** Conditions I (top left), II (top right), III (bottom left), and IV. We divide the trial-by-trial data into two equal-sized parts at random and find two memory relaxation times τ_m^* and τ_m^\diamond that accurately matches the average decision time for each respective portion of the experimental data. Points correspond to a scatter plot of these two parameters for each participant and lines with slope one to the ideal best fit.

Condition	Mean	Median
I	0.7438	0.5589
II	1.9105	1.1078
III	1.7156	1.3872
IV	2.9118	2.7146

TABLE S6: The global mean and median of τ_m^* (in seconds) averaged over all participants for different conditions.

Intrinsic decision threshold. We also compute the corresponding W_{dec} that generate L_W^* on a trial-by-trial basis for each participant using Eq. (S6). In Fig. S3, we plot the probability density of W_{dec} for a typical participant in the different conditions. The dashed lines represent the mean decision thresholds $-L_W^*$ and L_W^* with $L_W^* = \langle |W_{\text{dec}}| \rangle$. Note that the mean decision thresholds of EIM (L_W^*) change substantially with experimental conditions.

Accuracy. For each participant with its associated τ_m^* and L_W^* , the EIM overall yields similar predictions of accuracy to that of the SPRT (see Fig. S4).

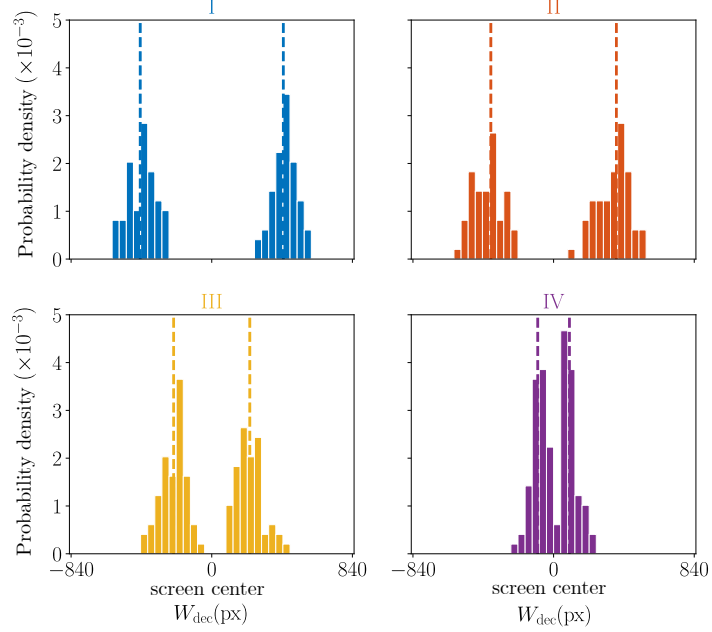


FIG. S3: **Probability density of $W_{\text{dec}} = W_{T_{\text{dec}}}$.** The histograms show the probability density of W_{dec} obtained from the trial-by-trial analysis of a single participant using Eq. (S6) across experimental conditions. The dashed lines in each condition display the corresponding mean values $-L_W^*$ and L_W^* .

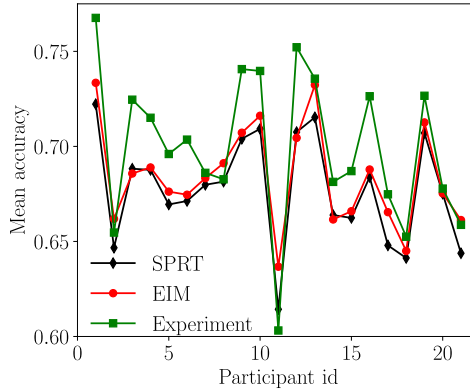


FIG. S4: **Participant-by-participant accuracy predictions.** Mean accuracy averaged over all experimental conditions, as a function of the participant's id. The EIM and the SPRT predict similar accuracy, and display correlation across subjects.

Kolmogorov-Smirnov (KS) Statistics. The KS statistical tests are also conducted to compare the predictions by the SPRT and the EIM. The KS test on EIM at a 95% confidence level yields significantly more accurate predictions on the experimental decision times T_{dec} with $D(11963)=0.103$ and $p = 0.421$ than that by the SPRT with $D(11963)=0.186$ and $p = 0.012$. A similar phenomenon is observed also for the predictions on the experimental decision thresholds X_{dec} , for which the same KS test on EIM yields $D(11963)=0.118$ and $p = 0.273$, while the SPRT gives $D(11963)=0.262$ and $p = 8.72 \times 10^{-5}$.

S5. VARIANCE OF DECISION THRESHOLD

We now explore the variance of decision threshold observed in Figs. 5C and 5D. To investigate the possible sources of the variance, we analyze consistency across participants. To proceed, let us denote the observed decision threshold of participant p in trial i for condition c by $X_{\text{dec}}^{p,c,i}$. For the participant p and condition c , we compute in each trial i

the relative difference between the decision threshold $X_{\text{dec}}^{p,c,i}$ and its average $\langle |X_{\text{dec}}^{p,c,j}| \rangle_j$ over all trials j :

$$\Delta X_{\text{dec}}^{p,c,i} \equiv \frac{\langle |X_{\text{dec}}^{p,c,j}| \rangle_j - |X_{\text{dec}}^{p,c,i}|}{\langle |X_{\text{dec}}^{p,c,j}| \rangle_j}. \quad (\text{S7})$$

We take an average of $\Delta X_{\text{dec}}^{p,c,i}$ over the participants, i.e., $\langle \Delta X_{\text{dec}}^{p,c,i} \rangle_p$, and plot it in Fig. S5 as a function of trials (i) .

We then calculate the null distribution of $\Delta X_{\text{dec}}^{p,c,i}$ by shuffling trials in order to find 95% confidence intervals, which are shown as the two fluctuating horizontal lines in the figure panels. Existence of low error bars of the data points and most of the trials being within the confidence interval imply consistency in decision thresholds across participants. The consistent responses of the participants for the same trial suggests that the variance in decision thresholds stems mostly from the fluctuations of the stimuli.

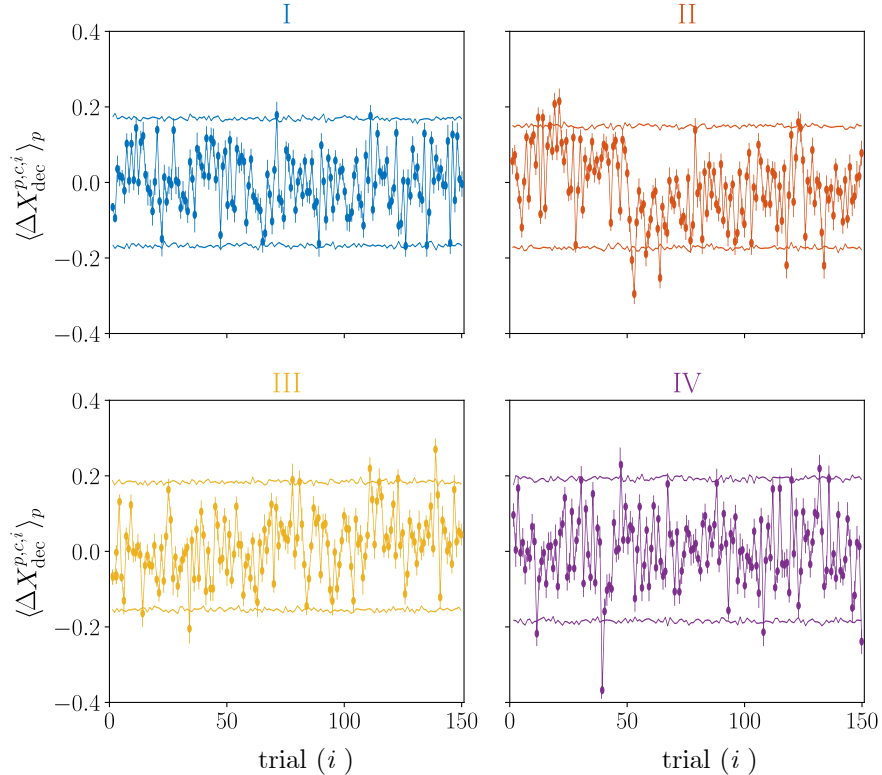


FIG. S5: **Participants respond consistently for the same trials.** Given the same trial (i) , we calculate the normalized change in each participant's decision threshold with respect to their mean. Each data point represents the mean of the normalized change over all participants. Error bars show the standard error of the mean. The fluctuating horizontal lines represent are set to 95% confidence intervals.

To investigate further the relation between the variance and stimuli, we conduct the control experiment explained in Sec. S1 with decision-free response tasks. From the outcomes of the no-diffusion (Fig. S6A) and Y -axis diffusion (Fig. S6B) versions of the control experiment, we observe substantially less variance in X -positions of the responses. Note that the stimuli in these two versions do not involve diffusion along the X -axis and, therefore, are fully deterministic along X . The observed variance thus could come from two sources: (i) the motor implementation in pressing the key and/or (ii) the spatio-temporal discreteness of the stimuli.

One may wonder what would be the case for a decision-free response task with stochastic stimuli where the trajectory of the disk is less predictable. To find an answer to this question, we conduct the original parameter version of the control experiment, where the same parameter values for the stimuli are used as the main experiment. Figure S7A shows the variance in the decision thresholds of the main experiment. On the other hand, Fig. S7B depicts the variance of the responses in the original parameter version of the control experiment. The behavior of the variance as a function of the entropy production rate is similar in both experiments. In both cases, the increase in the variance

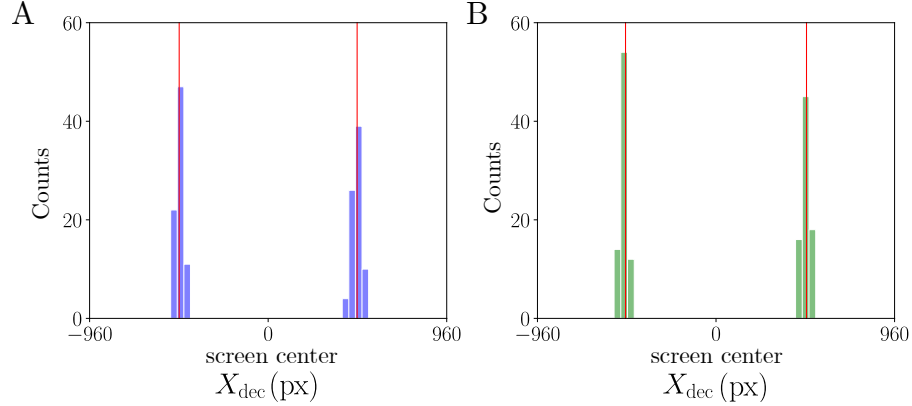


FIG. S6: **Control experiment results of an example participant.** (A) Control experiment, no diffusion version. The X -axis position of the disk at the moment of response shows very little variance. Participants are instructed to press the correspondent key (right/left) as soon as the disk reaches either of the visible red lines that are 500 pixels away from the center. The x -axis represents the horizontal axis of the screen with 1920 pixels. The red symmetrical lines are the borders that the participants see throughout the whole trial. y -axis is the number of observations of different positions of the disk at the response moment. (B) Control experiment, Y -axis diffusion version. The X -axis position of the disk at the moment of response shows very little variance. All participants show similar behavior. See Supplementary Sec. S1 for experiment details.

may be explained by (i) the higher instantaneous jumps and (ii) less predictability in the stimuli because of the higher entropy production rate. Importantly, the variance in the main experiment is significantly higher than that of the control experiment. So far in the different versions of control experiments, we discussed the potential non-decisional sources of the variance in decision thresholds. The difference between Figs. S7A and S7B tells us part of the variance in thresholds in the main decision task stems from cognitive decision processes. These cognitive decision processes that yield the variance in experimental data may be explained by the EIM. As we have discussed in Sec. V, Fig. 5D shows the predictability power of the EIM.

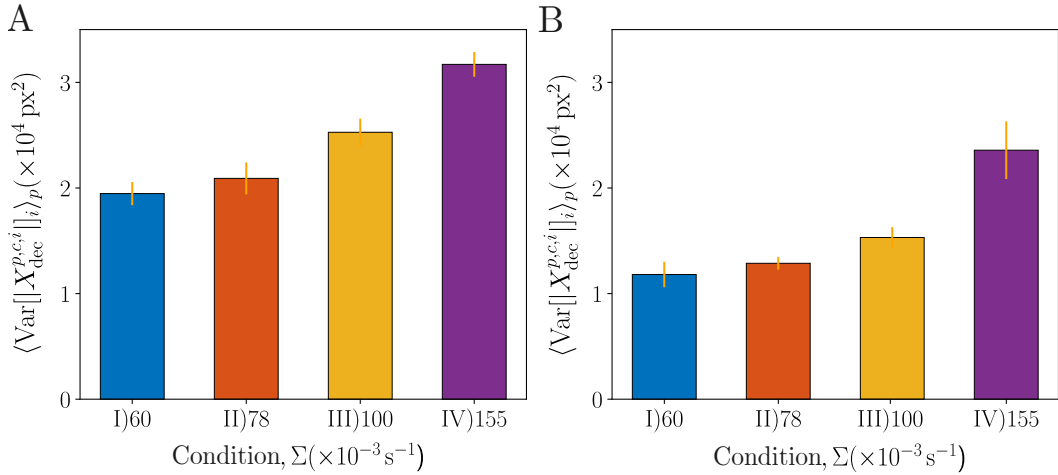


FIG. S7: **Variance in the X_{dec} .** (A) Experimental results from main experiment. The variance of X_{dec} averaged over participants across different experimental conditions. The variance in the decision threshold increases with entropy production rate. (B) Experimental results from the control experiment original parameters version. Participants are instructed to press the decision key as soon as the disk reaches visible red lines in the screen, representing Wald's SPRT-like fixed thresholds. Even though overall variance is decreased as opposed to the main experiment in panel A, there is still some variance, and it varies across conditions in a similar pattern like in panel A.

S6. CROSS-VALIDATION OF MEAN DECISION TIMES

In order to test the robustness of the decision thresholds in predicting the decision times, we perform a cross-validation for each participant in each condition. We divide the trial-by-trial data into two equal-sized segments at random (training and test) and use the mean decision thresholds of the training data to predict T_{dec} for the test data. Note that for the case of EIM to obtain the decision threshold we use τ_m^* on the trials of the training set. We find that the experimental mean decision time of the training data accurately matches the predicted mean decision time of the test data for both SPRT (see Fig. S8A) and EIM (see Fig. S8B). This suggests that the knowledge of decision thresholds of a particular data set may be used in predicting the decision times of unseen data.

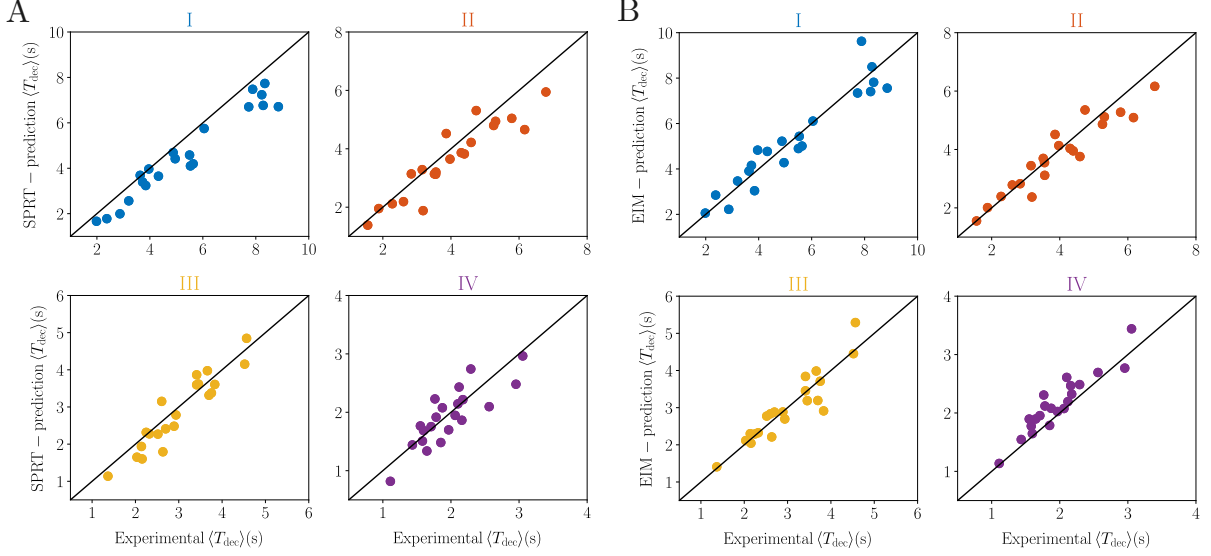


FIG. S8: **Cross validation of the model predictions of T_{dec} for (A) SPRT, and (B) EIM.** We find that the average experimental decision time of the training data accurately matches the predicted decision time of the test data for both (A) SPRT and (B) EIM. Each data point represents participants and the lines the best prediction.

[1] Gold, J. I., Shadlen, M. N. *et al.* The neural basis of decision making. *Annu. Rev. Neurosci.* **30**, 535–574 (2007).

[2] Wald, A. Sequential tests of statistical hypotheses. *Ann. Math. Stat.* **16**, 117–186 (1945).

[3] Tartakovsky, A., Nikiforov, I. & Basseville, M. *Sequential Analysis: Hypothesis Testing and Changepoint Detection* (CRC press, London, 2015).

[4] Wald, A. & Wolfowitz, J. Optimum character of the sequential probability ratio test. *Ann. Math. Stat.* 326–339 (1948).

[5] Sigsga, E. D. & Vergassola, M. Decisions on the fly in cellular sensory systems. *Proc. Natl. Acad. Sci. U.S.A.* **110**, E3704–E3712 (2013).

[6] Desponts, J., Vergassola, M. & Walczak, A. M. A mechanism for hunchback promoters to readout morphogenetic positional information in less than a minute. *eLife* **9**, e49758 (2020).

[7] Ratcliff, R., Smith, P. L., Brown, S. D. & McKoon, G. Diffusion decision model: Current issues and history. *Trends Cogn. Sci.* **20**, 260–281 (2016).

[8] Ratcliff, R. & McKoon, G. The diffusion decision model: theory and data for two-choice decision tasks. *Neural Comput.* **20**, 873–922 (2008).

[9] Forstmann, B. U., Ratcliff, R. & Wagenmakers, E.-J. Sequential sampling models in cognitive neuroscience: Advantages, applications, and extensions. *Annu. Rev. Psychol.* **67**, 641 (2016).

[10] Ratcliff, R., Smith, P. L. & McKoon, G. Modeling regularities in response time and accuracy data with the diffusion model. *Curr. Dir. Psychol. Sci.* **24**, 458–470 (2015).

[11] Salzman, C. D., Britten, K. H. & Newsome, W. T. Cortical microstimulation influences perceptual judgements of motion direction. *Nature* **346**, 174–177 (1990).

[12] Shadlen, M. N. & Newsome, W. T. Neural basis of a perceptual decision in the parietal cortex (area lip) of the rhesus monkey. *J. Neurophysiol.* **86**, 1916–1936 (2001).

[13] Roitman, J. D. & Shadlen, M. N. Response of neurons in the lateral intraparietal area during a combined visual discrimination reaction time task. *J. Neurosci.* **22**, 9475–9489 (2002).

[14] Rigosa, J. *et al.* Dye-enhanced visualization of rat whiskers for behavioral studies. *eLife* **6**, e25290 (2017).

[15] Gerstner, W., Kistler, W. M., Naud, R. & Paninski, L. *Neuronal Dynamics: From Single Neurons to Networks and Models of Cognition* (Cambridge University Press, Cambridge, 2014).

[16] Park, H., Lueckmann, J.-M., von Kriegstein, K., Bitzer, S. & Kiebel, S. J. Spatiotemporal dynamics of random stimuli account for trial-to-trial variability in perceptual decision making. *Sci. Rep.* **6**, 1–17 (2016).

[17] Fard, P. R., Bitzer, S., Pannasch, S. & Kiebel, S. J. Stochastic motion stimuli influence perceptual choices in human participants. *Front. Neurosci.* **15**, 1893 (2022).

[18] Insabato, A., Dempere-Marco, L., Pannunzi, M., Deco, G. & Romo, R. The influence of spatiotemporal structure of noisy stimuli in decision making. *PLoS Comput. Biol.* **10**, e1003492 (2014).

[19] Wimmer, K. *et al.* Sensory integration dynamics in a hierarchical network explains choice probabilities in cortical area mt. *Nat. Commun.* **6**, 6177 (2015).

[20] Urai, A. E., Braun, A. & Donner, T. H. Pupil-linked arousal is driven by decision uncertainty and alters serial choice bias. *Nat. Commun.* **8**, 14637 (2017).

[21] Zylberberg, A., Barttfeld, P. & Sigman, M. The construction of confidence in a perceptual decision. *Front. Integr. Neurosci.* **6**, 79 (2012).

[22] Kiani, R., Hanks, T. D. & Shadlen, M. N. Bounded integration in parietal cortex underlies decisions even when viewing duration is dictated by the environment. *J. Neurosci.* **28**, 3017–3029 (2008).

[23] Peixoto, D. *et al.* Decoding and perturbing decision states in real time. *Nature* **591**, 604–609 (2021).

[24] Brunton, B. W., Botvinick, M. M. & Brody, C. D. Rats and humans can optimally accumulate evidence for decision-making. *Science* **340**, 95–98 (2013).

[25] Mora, T. & Wingreen, N. S. Limits of sensing temporal concentration changes by single cells. *Physical review letters* **104**, 248101 (2010).

[26] ten Wolde, P. R., Becker, N. B., Ouldridge, T. E. & Mugler, A. Fundamental limits to cellular sensing. *Journal of Statistical Physics* **162**, 1395–1424 (2016).

[27] Fang, X., Kruse, K., Lu, T. & Wang, J. Nonequilibrium physics in biology. *Rev. Mod. Phys.* **91**, 045004 (2019).

[28] Roldán, É., Neri, I., Dörpinghaus, M., Meyr, H. & Jülicher, F. Decision making in the arrow of time. *Phys. Rev. Lett.* **115**, 250602 (2015).

[29] Seifert, U. Entropy production along a stochastic trajectory and an integral fluctuation theorem. *Phys. Rev. Lett.* **95**, 040602 (2005).

[30] Redner, S. *A Guide to First-Passage Processes* (Cambridge university press, Cambridge, 2001).

[31] Barato, A. C. & Seifert, U. Thermodynamic uncertainty relation for biomolecular processes. *Phys. Rev. Lett.* **114**, 158101 (2015).

[32] Gingrich, T. R., Horowitz, J. M., Perunov, N. & England, J. L. Dissipation bounds all steady-state current fluctuations. *Phys. Rev. Lett.* **116**, 120601 (2016).

[33] Falasco, G. & Esposito, M. Dissipation-time uncertainty relation. *Phys. Rev. Lett.* **125**, 120604 (2020).

[34] Horowitz, J. & Gingrich, T. Thermodynamic uncertainty relations constrain non-equilibrium fluctuations. *Nat. Phys.* **16**, 15–20 (2020).

[35] Neri, I. Universal tradeoff relation between speed, uncertainty, and dissipation in nonequilibrium stationary states. *SciPost*

Phys. (2021).

[36] Ossmy, O. *et al.* The timescale of perceptual evidence integration can be adapted to the environment. *Current biology* **23**, 981–986 (2013).

[37] Glaze, C. M., Kable, J. W. & Gold, J. I. Normative evidence accumulation in unpredictable environments. *Elife* **4**, e08825 (2015).

[38] Piet, A. T., El Hady, A. & Brody, C. D. Rats adopt the optimal timescale for evidence integration in a dynamic environment. *Nature communications* **9**, 4265 (2018).

[39] Seif, A., Hafezi, M. & Jarzynski, C. Machine learning the thermodynamic arrow of time. *Nat. Phys.* **17**, 105–113 (2021).

[40] Lynn, C. W., Cornblath, E. J., Papadopoulos, L., Bertolero, M. A. & Bassett, D. S. Broken detailed balance and entropy production in the human brain. *Proc. Natl. Acad. Sci. U.S.A.* **118**, e2109889118 (2021).

[41] Wong, K.-F. & Huk, A. C. Temporal dynamics underlying perceptual decision making: Insights from the interplay between an attractor model and parietal neurophysiology. *Front. Neurosci.* **2**, 383 (2008).

[42] Wang, X.-J. Probabilistic decision making by slow reverberation in cortical circuits. *Neuron* **36**, 955–968 (2002).

[43] Wong, K.-F. & Wang, X.-J. A recurrent network mechanism of time integration in perceptual decisions. *J. Neurosci.* **26**, 1314–1328 (2006).

[44] G-Guzmán, E. *et al.* The lack of temporal brain dynamics asymmetry as a signature of impaired consciousness states. *Interface Focus* **13**, 20220086 (2023).

[45] de la Fuente, L. A. *et al.* Temporal irreversibility of neural dynamics as a signature of consciousness. *Cereb. Cortex* **33**, 1856–1865 (2023).

[46] Cruzat, J. *et al.* Temporal irreversibility of large-scale brain dynamics in Alzheimer’s disease. *J. Neurosci.* **43**, 1643–1656 (2023).

[47] Zanin, M., Güntekin, B., Aktürk, T., Hanoğlu, L. & Papo, D. Time irreversibility of resting-state activity in the healthy brain and pathology. *Front. physiol.* **10**, 1619 (2020).

[48] Bates, D., Mächler, M., Bolker, B. & Walker, S. Fitting linear mixed-effects models using lme4. *J. Stat. Softw.* **67** (2015).

[49] Additionally, statistics of y -coordinates are also stored, and tested for, among other things show that the information about the y coordinate did not add up significant weight of evidence in participants’ decisions.

[50] We implement reflecting boundary conditions along the y -axis of the screen. In other words, the disk bounces back to its previous position when it touches any of its edges along the y -axis. For our analyses, we have discarded all the trials where the disk crosses any screen border before the participants take his/her decision.